CrossMark

The Morphology and Dynamics of Relativistic Jets with Relativistic Equation of State

Raj Kishor Joshi[1,2] and Indranil Chattopadhyay[1]

[1] Aryabhatta Research Institute of Observational Sciences (ARIES), Manora Peak, Nainital 263001, India; indra@aries.res.in
[2] Department of Physics, Deen Dayal Upadhyay Gorakhpur University, Gorakhpur, 273009, India

Abstract

We study the effect of plasma composition on the dynamics and morphology of relativistic astrophysical jets. Our work is based on a relativistic total variation diminishing simulation code. We use a relativistic equation of state in the simulation code that accounts for the thermodynamics of a multispecies plasma, which is a mixture of electrons, positrons, and protons. To study the effect of plasma composition, we consider various jet models. These models are characterized by the same injection parameters, same jet kinetic luminosity, and the same Mach numbers. The evolution of these models shows that the plasma composition affects the propagation speed of the jet head, the structure of the jet head, and the morphology, despite fixing the initial parameters. We conclude that electron-positron jets are the slowest and show more pronounced turbulent structures in comparison to other plasma compositions. The area and locations of the hot-spots also depend on the composition of the jet plasma. Our results also show that boosting mechanisms are an important aspect of multi-dimensional simulations, which are also influenced by the change in composition.

Unified Astronomy Thesaurus concepts: Relativistic jets (1390); Relativistic fluid dynamics (1389)

1. Introduction

Collimated relativistic outflows or jets are a common feature of active galactic nuclei (AGNs) as well as of microquasars (i. e., an X-ray binary where a stellar-mass black hole or neutron star is the primary and a normal star is the secondary). These jets carry a large amount of kinetic energy, which is transported away from the center of gravity. Many of these jets are radio bright. Depending upon the energy, the radio emitting extragalactic jets (i. e., from AGN) are classified into two categories, namely FR-I and FR-II (Fanaroff & Riley 1974). The FR I are low luminosity jets with brighter structures close to the nucleus. The FR II sources have powerful jets and their maximum brightness is at the regions of jet termination. Apart from the difference in power, possibly the interaction between the jet beam and external medium, the effect of entrainment and mixing due to different types of jet instabilities (Rossi et al. 2020) also plays a significant role in shaping the FR-I and FR-II morphology. Our understanding of the morphology and dynamics of the jets has been significantly improved by analytical (Blandford & Rees 1974; Komissarov 1994; Kawakatu & Kino 2006; Bromberg et al. 2011) and numerical studies (Martí et al. 1997; Mioduszewski et al. 1997; Mizuta et al. 2004; Seo et al. 2021). These numerical simulations show that the jets produce complex structures with shocks, backflow, and instabilities when they interact with the ambient medium. The growth in computational power and improvement in numerical algorithms have given a tremendous boost to this subject. The high-resolution shock capturing (HRSC) simulation methods (Duncan & Hughes 1994; Marti et al. 1994; Walg et al. 2013) improved our understanding of the morphology of relativistic jets. Recently, the numerical studies have been expanded to include the effect of the magnetic field on jet dynamics through magnetohydrodynamic (MHD) simulations

(Keppens et al. 2008; Mignone et al. 2010; Hardcastle & Krause 2014; Komissarov & Porth 2021). Numerical simulation codes solve the set of conservation laws along with an equation of state (EoS), which relates the thermodynamic variables such as internal energy, pressure, and mass density. Most of the simulation codes are based on the ideal gas EoS, in which the adiabatic index remains a constant parameter (4/3 for hot gas and 5/3 for cold gas). This EoS is a reasonable approximation if the flow remains ultra-relativistic or non-relativistic throughout its evolution. However, for astrophysical jets that span over very large length scales and vary over a large span of temperatures and propagation velocities, the use of fixed adiabatic index EoS is not physically consistent. Jets also exhibit strong shocks where the gas is heated to extreme temperatures. In the context of astrophysical jets, Duncan et al. (1996) highlighted the importance of using an EoS which self-consistently calculates the adiabatic index. The EoS for relativistic fluid has been computed independently by several authors (Chandrasekhar 1939; Synge 1957). However, the expressions for these EoS involve complicated modified-Bessel functions; hence, their implementation in the simulation codes is a complicated task and it also increases the computational cost (Falle & Komissarov 1996). To avoid this extra computational cost and numerical difficulties, many algebraic approximations have been proposed (Mathews 1971; Mignone et al. 2005; Ryu et al. 2006) for the relativistic EoS. These EoS self-consistently calculate the adiabatic index from the information of temperature and account for the transition between cold to hot thermal states (and vice versa) in a consistent manner. It has been shown that the EoS proposed by Ryu et al. (2006) mimics the one by Chandrasekhar extremely well. The EoS proposed by Ryu et al. (2006) was extended by Chattopadhyay & Ryu (2009; abbreviated as CR EoS) for the plasma composed of dissimilar particles. CR EoS can account for a mixture of electrons, positrons, and protons, which allows us to study the effect of plasma composition on the dynamics of astrophysical flows. CR EoS has been used in many analytical investigations and the effect of plasma composition has been

studied (Chattopadhyay & Chakrabarti 2011; Chattopadhyay & Kumar 2016; Singh & Chattopadhyay 2019; Sarkar et al. 2020; Joshi et al. 2022a; Sarkar & Chattopadhyay 2022). However, to date, there is a lack of numerical investigations of the effect of plasma composition on jet dynamics (with the notable exception of Scheck et al. 2002). In our previous analytical investigation (Joshi et al. 2021), we obtained the exact solution of a one-dimensional jet using CR EoS. We investigated when a Riemann problem will behave like a jet (forward shock or FS —Contact discontinuity or CD—reverse shock or RS) and when it will behave like a shock tube test (FS—CD— rarefaction fan or RF). We also studied the effect of plasma composition on the propagation speed of the jet head and on the shock dynamics. Based on the algorithms of Ryu et al. (2006) and Chattopadhya et al. (2013), we developed a one-dimensional relativistic code that incorporates gravity in the weak field limit to study radiatively driven, transonic, relativistic jets around black holes (Joshi et al. 2022b). In this paper, we extend the work of Joshi et al. (2021) to two-dimensional axis-symmetric relativistic jet simulations. The metric is special relativistic but in cylindrical geometry in the space dimension. In multi-dimensions, the injected jet material is deflected back and interacts with the injected jet material. Therefore, the evolution of morphology is likely to be quite different from the one-dimensional study. We do see in multi-dimensional simulations that the propagation speed of the jet head (CD) can be higher or lower than the one-dimensional estimate, depending on how many RFs are produced. We would like to study it while using the CR EoS. Moreover, we ask if the creation of RFs is also affected by jet composition, which therefore affects the jet propagation speed? In this paper, we study jet dynamics in general, and in particular the effect of plasma composition on jet physics. This paper is organized as follows. In Section 2, we describe the governing equations, the details of the simulation setup, and CR EoS. In Section 3.1, we discuss the results describing the morphology and dynamics of the jet. Section 3.3 will show the effect of plasma composition on the jet's morphology. A brief discussion and conclusion of the work are given in Section 4.

2. Numerical Setup and Governing Equations

We solve the relativistic hydrodynamic equations in two-dimensional cylindrical geometry (r,z) and the three velocity vector is given by $v \equiv (v^r, 0, v^z)$. We use a uniform spacing grid $\Delta r = \Delta z = $ constant to discretize the computational domain in 750×6000 cells. In code units, this domain is of size $r = 5$, $z = 40$. The reflection boundary condition is imposed along the z-axis. The initial jet beam is resolved by 10×10 cells, so the computational domain covers a region of $75 r_b \times 600 r_b$. The jet material is continuously injected using a fixed jet base. The outer r and z boundaries are kept as outflow boundaries. Assuming a beam size $r_b = 0.4$ kpc, the computational domain covers 30 kpc × 240 kpc. The unit time in code is equal to 2×10^4 yr. The injected jet material travels through a dense, static ambient medium, and the density of the ambient medium is kept constant. We have performed simulations for various jet parameters, which are listed in Table 1. The injection velocity $v_j = 0.995$, which corresponds to injection beam Lorentz factor $\gamma_j = 10$, is kept same for all of the models. The time evolution of the jet material is governed by the

following equations:

$$\frac{\partial D}{\partial t} + \frac{1}{r}\frac{\partial}{\partial r}[rDv^r] + \frac{\partial}{\partial z}[Dv^z] = 0 \qquad (1a)$$

$$\frac{\partial M^r}{\partial t} + \frac{1}{r}\frac{\partial}{\partial r}r[M^r v^r + p] + \frac{\partial}{\partial z}[M^r v^z] = \frac{p}{r} \qquad (1b)$$

$$\frac{\partial M^z}{\partial t} + \frac{1}{r}\frac{\partial}{\partial r}r[M^z v^r] + \frac{\partial}{\partial z}[M^z v^z + p] = 0 \qquad (1c)$$

$$\frac{\partial E}{\partial t} + \frac{1}{r}\frac{\partial}{\partial r}r[(E + p)v^r] + \frac{\partial}{\partial z}[(E + p)v^z] = 0, \qquad (1d)$$

where D, M^r, M^z, E are the conserved quantities, namely the mass density, radial and axial component of momentum density, and total energy density, respectively. These quantities are measured in a laboratory frame and these are related with primitive variables as

$$D = \rho\gamma \qquad (2a)$$

$$M^{r,z} = \gamma^2 \rho h v^{r,z} \qquad (2b)$$

$$E = \gamma^2 \rho h - p. \qquad (2c)$$

The variables ρ, p, h denote proper rest mass density, pressure, and specific enthalpy, respectively. Meanwhile, v^r and v^z are the radial and axial components of the velocity, which are related with the Lorentz factor as

$$\gamma = \frac{1}{\sqrt{1 - v^2}} \qquad \text{with } v^2 = (v^r)^2 + (v^z)^2. \qquad (3)$$

To solve the set of Equations (1a)–(1d), we need an additional equation as a closure relation. This closure equation is commonly known as the EoS.

2.1. Equation of State

The EoS relates the thermodynamic variables such as internal energy density, rest mass density, and pressure. Most of the analytical and numerical studies use an ideal gas with a fixed adiabatic index. However, fixing the adiabatic index can be a reasonable approximation only if the flow remains either ultra-relativistic or non-relativistic. In the case of astrophysical jets, the use of ideal gas EoS will be inconsistent because the jets cover a very long distance and the temperature varies significantly. In addition, the relativistic jets are known to have multiple shock-heated regions, which will contain thermally relativistic gas. Hence, it is desirable to use an EoS that accounts for self consistent evolution of the adiabatic index (Duncan et al. 1996). We use CR EoS (Chattopadhyay & Ryu 2009) for relativistic multispecies fluid, which is a very close fit to the exact EoS derived by Chandrasekhar (1939). The EoS is in the form

$$e = \rho f, \qquad (4)$$

where

$$f = 1 + (2 - \xi)\Theta\left[\frac{9\Theta + 6/\tau}{6\Theta + 8/\tau}\right] + \xi\Theta\left[\frac{9\Theta + 6/\eta\tau}{6\Theta + 8/\eta\tau}\right]. \qquad (5)$$

The mass density of fluid given as $\rho = \Sigma_i n_i m_i = n_{e^-}m_e(2 - \xi + \xi/\eta)$, where $\xi = n_p/n_{e^-}$, $\eta = m_e/m_p$ and n_{e^-}, n_p, m_e and m_p are the electron number density, the proton number density, the electron rest mass, and proton rest mass,

Table 1
Details of the Jet and Ambient Medium Parameters Used in the Jet Simulations

Model	ρ_j	Θ_j	$\mathcal{M}$	h_j	ξ	$L_j(\mathrm{erg\ s^{-1}})$	ρ_a	Θ_a	h_a
OD	1.0	0.02	59.66	1.06	1.00	1.02×10^{45}	2×10^3	1×10^{-5}	1.00002
A1	1.0	0.20	20.69	1.57	0.00	3.04×10^{45}	1×10^3	1×10^{-4}	1.000250
A2	1.0	0.20	23.42	1.76	0.20	3.41×10^{45}	1×10^3	1×10^{-4}	1.000253
A3	1.0	0.20	22.89	1.73	0.50	3.35×10^{45}	1×10^3	1×10^{-4}	1.000257
A4	1.0	0.20	22.05	1.67	1.00	3.23×10^{45}	1×10^3	1×10^{-4}	1.000259
B1	1.0	0.49	16.33	2.54	0.00	4.92×10^{45}	1×10^3	5.62×10^{-4}	1.0014
B2	1.0	0.40	19.13	2.54	0.20	4.92×10^{45}	1×10^3	5.27×10^{-4}	1.0014
B3	1.0	0.42	18.41	2.54	0.50	4.92×10^{45}	1×10^3	5.04×10^{-4}	1.0014
B4	1.0	0.45	17.47	2.54	1.00	4.92×10^{45}	1×10^3	5.01×10^{-4}	1.0014
C1	1.0	0.20	21.0	1.57	0.00	3.03×10^{45}	1×10^3	1.00×10^{-4}	1.000250
C2	1.0	0.29	21.0	2.15	0.20	4.16×10^{45}	1×10^3	1.02×10^{-4}	1.000258
C3	1.0	0.27	21.0	2.00	0.50	3.87×10^{45}	1×10^3	1.03×10^{-4}	1.000265
C4	1.0	0.24	21.0	1.82	1.00	3.52×10^{45}	1×10^3	1.04×10^{-4}	1.000269

Note. The variables $\rho_j(\rho_a)$, $\Theta_j(\Theta_a)$, $h_j(h_a)$, $\mathcal{M}$, L_j represent the jet (ambient) mass density, jet (ambient) dimensionless temperature, jet (ambient) specific enthalpy, relativistic Mach number of jet beam, and the kinetic luminosity of the jet, respectively.

respectively. $\Theta = p/\rho$ is a measure of temperature and $\tau = 2 - \xi + \xi/\eta$. The expressions for the sound speed and polytropic index are given as

$$a^2 = \frac{1}{h}\frac{\partial p}{\partial \rho} = -\frac{\rho}{Nh}\frac{\partial h}{\partial \rho} = \frac{\Gamma\Theta}{h} \qquad (6)$$

$$N = \rho\frac{\partial h}{\partial p} - 1 = \frac{\partial f}{\partial \Theta} = 6\left[(2 - \xi)\frac{9\Theta^2 + 24\Theta/\tau + 8/\tau^2}{(6\Theta + 8/\tau)^2}\right]$$
$$+ 6\xi\left[\frac{9\Theta^2 + 24\Theta/(\eta\tau) + 8/(\eta\tau)^2}{\{6\Theta + 8/(\tau\eta)\}^2}\right]. \qquad (7)$$

The adiabatic index is related with the polytropic index as $\Gamma = 1 + \frac{1}{N}$, which will be a function of Θ.

The set of relativistic hyperbolic conservation laws (1a)–(1d) is solved using a relativistic total variation diminishing (TVD) routine. Originally, the TVD scheme was proposed to solve the set of non-relativistic hydrodynamic conservation laws (Harten 1983). The relativistic TVD simulation code to incorporate the relativistic EoS has been built previously (Ryu et al. 2006; Chattopadhya et al. 2013). A detailed description of how the code was built for a general EoS is given in Ryu et al. (2006). The one-dimensional relativistic TVD code with CR EoS has also been recently used to study the radiatively driven relativistic jets (Joshi et al. 2022b).

3. Results

The jet is characterized as a narrow beam of hot and relativistic material traveling through the cold and denser ambient medium. In Model OD, we present the basic structure of a relativistic jet plying through the ambient medium. The initial surface of discontinuity between the jet material and the ambient medium is the CD or the working surface. The supersonic jet material drives a shock (FS) in the ambient medium. The jet beam also contains a shock (RS), behind the contact discontinuity, where the bulk kinetic energy of the jet beam is converted into thermal energy. As the jet advances and sweeps up the ambient medium in front and drives the FS, a backflow starts to develop around the jet beam. This backflow is an important feature of highly supersonic jets. In this paper, we have studied three basic models: Models A1–A4 are jet

models with the same injection parameters but we compare solutions with different compositions; Models B1–B4 are jets with the same enthalpy and jet power; and Models C1–C4 are jets with the same Mach number and their initial parameters are tabulated in Table 1.

3.1. Model OD: The Large Scale Morphology of The Jet

In Figure 1, we have plotted the density contours along with the velocity vector field (white arrows) in the r-z plane at different epochs to show the evolution of the jet of Model OD. The supersonic jet advancing in a denser ambient medium drives a bow shock FS. The ambient medium material ahead of the jet head is pushed in the transverse direction, which leads to the formation of the overpressured and hot cocoon around the jet beam. In the initial phase of evolution, the jet remains thin and propagates as a very narrow beam of relativistic plasma. As the jet plows through the ambient medium, the jet head starts to expand and it develops backflow, as shown in Figure 1(b). The zoomed inset in Figure 1(c) shows the structure of the jet head, and the location of FS, CD, and RS are shown in the inset. The sideways expansion and the formation of turbulent structures significantly reduce the propagation speed of the jet. Further in time at $t \sim 4$ Myr and $t \sim 11.6$ Myr, the interaction of the backflow and the jet beam intensifies, which causes the formation of multiple shocks and a lot of structures start to form in the jet beam. In Figure 1(d), one can clearly see that the interaction of back-flowing jet material with the jet beam results in perturbations in fluids and these perturbations grow into the Kelvin–Helmholtz instability (Norman et al. 1982), which are transported back toward the jet nozzle as the jet advances ahead. The formation of a vortex along the jet head and sideways expansion is clearly visible from the density contours (Figure 1(d)).

3.2. The Thermodynamic Variables

It follows from Equations (4)–(7) that any change in composition or Θ will affect the thermodynamic quantities, such as the enthalpy, the sound speed, and the adiabatic index. In Figures 2(a)–(c), we have plotted Γ, h, and c_s as a function of Θ, respectively. The composition parameter ξ is mentioned in the figure. It is very clear that for $\Theta > 1$, $\Gamma \rightarrow 4/3$ and for low values of Θ, $\Gamma \rightarrow 5/3$, for any values of ξ. However, for
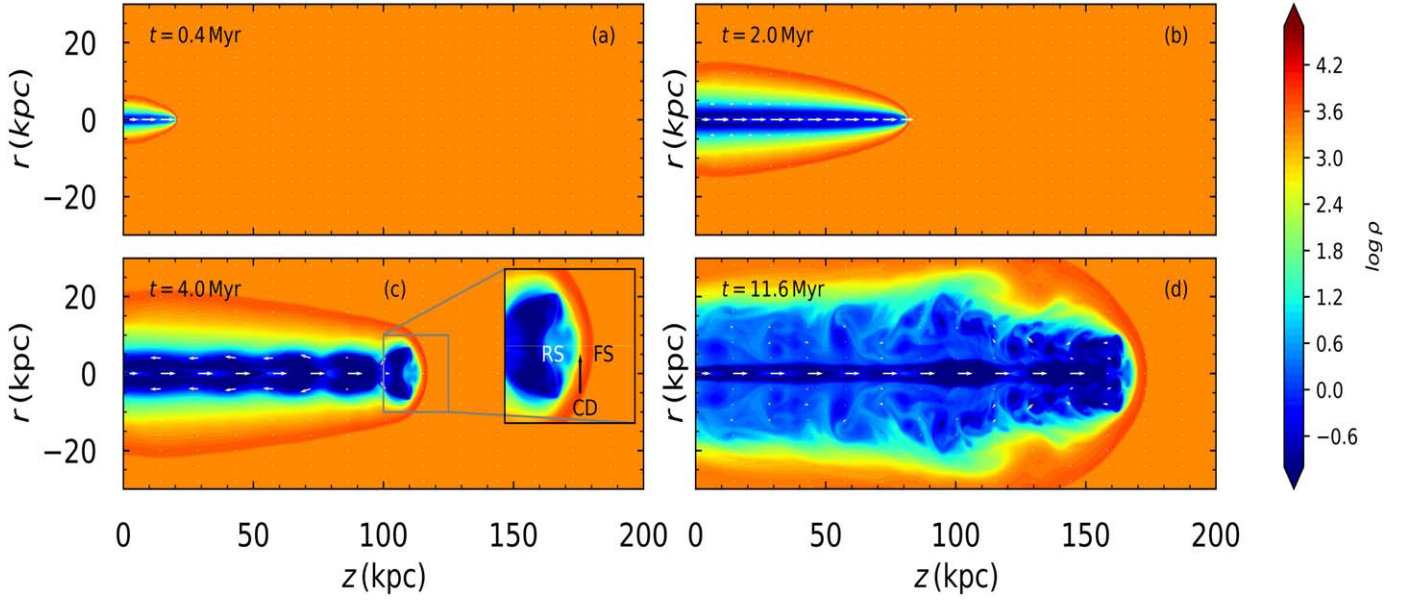
Figure 1. The density contours along with velocity vectors at various time steps, as mentioned in the four panels (a—$t = 0.4$ Myr, b—$t = 2.0$ Myr, c—$t = 4.0$ Myr and d—$t = 11.6$ Myr), for jet Model OD. In panel (c), the FS, CD (jet head), and RS are shown. The jet is composed of electrons and protons or $\xi = 1$.
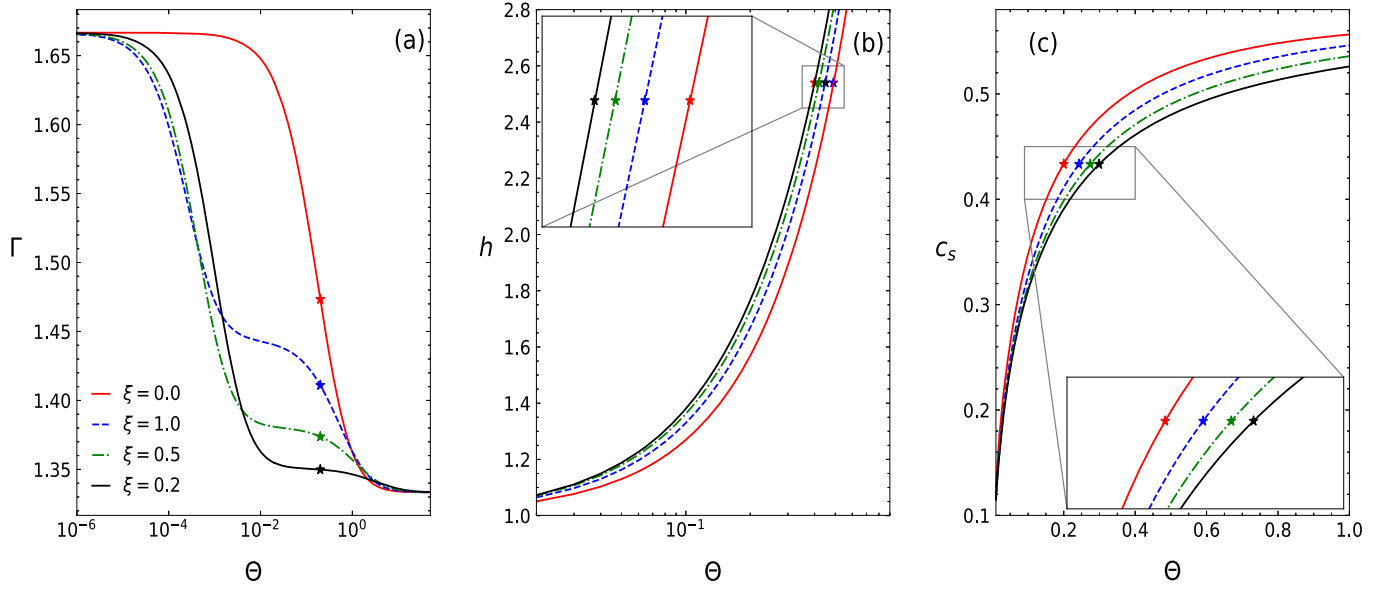

Figure 2. The adiabatic index Γ (a), enthalpy h (b), and sound speed c_s (c) as a function of Θ for various plasma compositions.

intermediate values, Γ depends on the composition of the gas. Since Γ is the comparison of the random kinetic energy of the gas particles compared to the inertia of the same particles, its lower value indicates that the gas is thermally relativistic. At a given Θ, the value of Γ does not monotonically change with ξ. In some Θ range, $\xi = 0.2$ is thermally the most relativistic; while at some other range, $\xi = 0.5$ is more relativistic. The stars on the curves in Figure 2(a), indicate the injection values of the jet in Models A1–A4. Similarly, h is lowest for $\xi = 0.0$ gas, while for $\xi = 0.2$ it is highest for most values of Θ. So, to attain the same value of h, the pair plasma needs to be very hot. Conversely, for a given value of Θ, c_s is highest for $\xi = 0.2$. The stars in Figure 2(b) are the injection values for the jet in Models B1–B4. Similarly, the stars in panel (c) are the injection parameters for Models C1–C4.

3.3. Model A: Same Injection Parameters

The evolution of the jet is characterized by the injection velocity, the injected pressure, and density. In Models A1–A4, we have kept the same injection values for velocity, pressure, and density v_j, p_j, and ρ_j (see Table 1). The difference between the models is in the composition of the flow: in Model A1, it is $\xi = 0$; for A2 it is $\xi = 0.2$, in A3 $\xi = 0.5$; and for A4 it is $\xi = 1.0$. The stars in Figure 2(a) show the values of the injection parameters that are used for the simulation of Models A1–A4. Despite fixing the value of Θ, we can see that the various models have different sound speeds (hence, different Mach numbers) and also a difference in the adiabatic index. In Figures 3(a)–(d), we have plotted the density contours and velocity vectors of Models A1–A4. All of the panels are plotted at $t = 10.8$ Myr. Model A2 with composition $\xi = 0.2$ is the
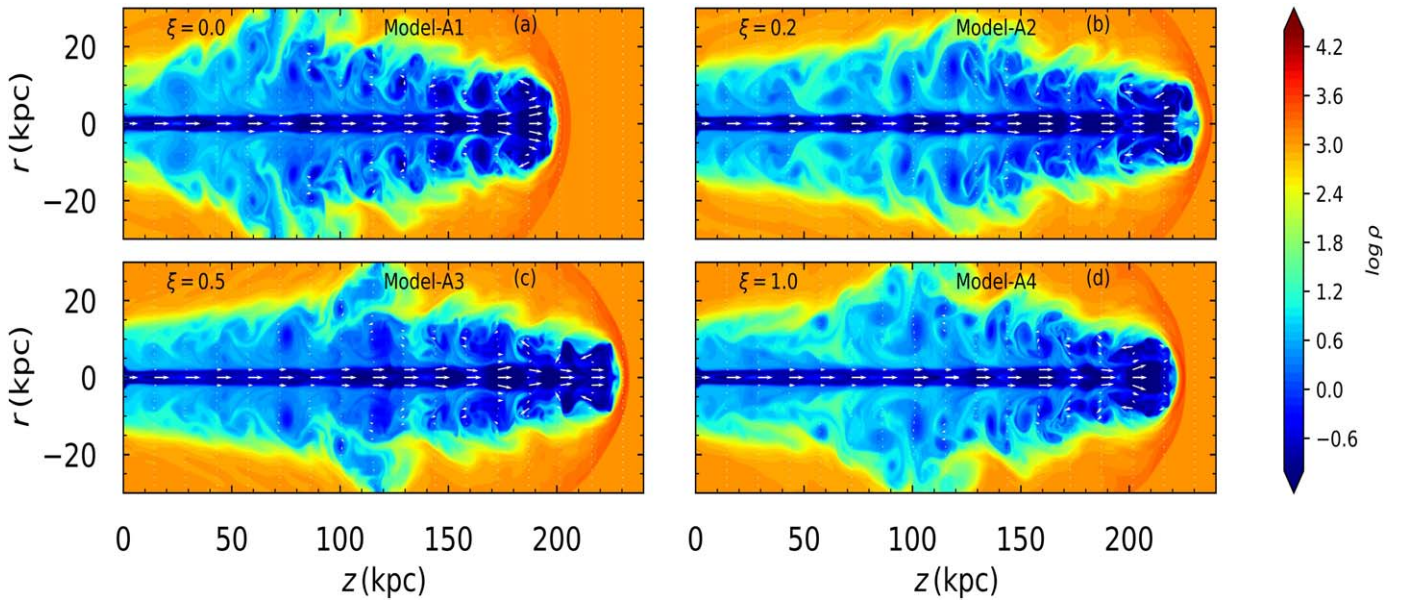
Figure 3. The contours of logarithmic density ($\log \rho$) along with velocity vectors for various compositions. The injection parameters ρ_j, Θ_j are kept the same for all of the jet models.
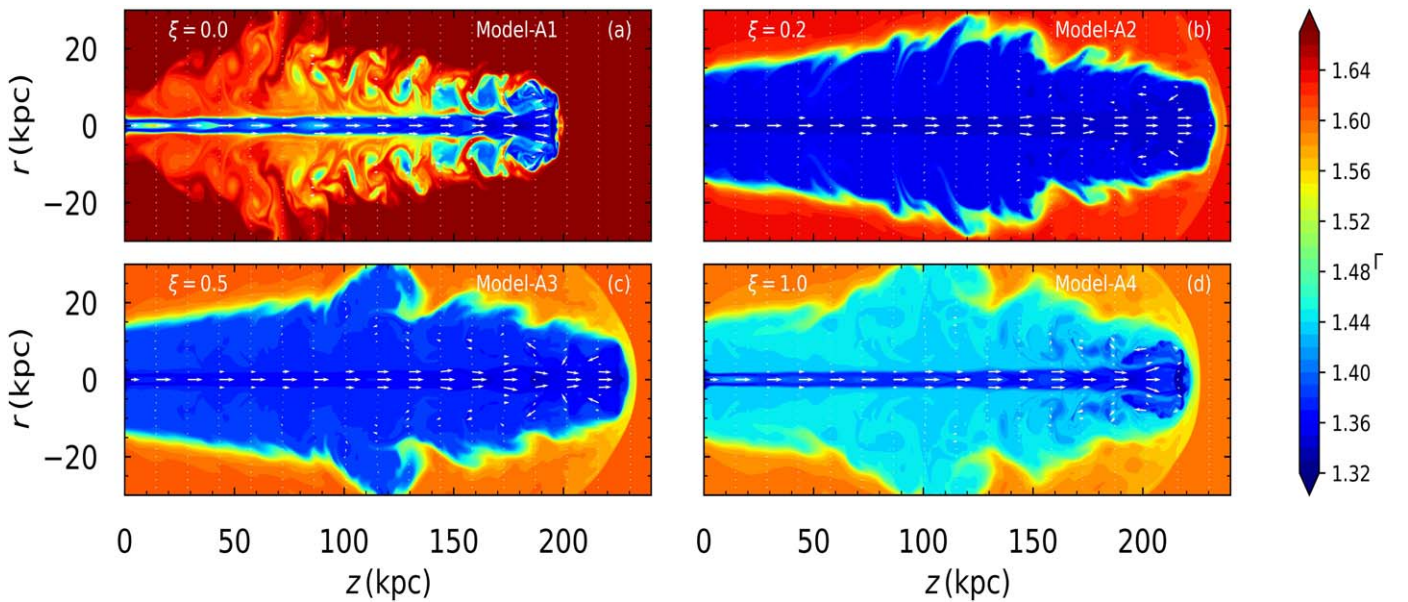

Figure 4. Contours of adiabatic index for different models (A1–A4) at $t = 10.8$ Myr.

fastest and has the highest jet kinetic power. Pair plasma or $\xi = 0.0$ jet has the slowest propagation speed. The large scale vortices form at an earlier time for the pair-plasma jet, and hence it loses the thrust forward, which results in a slower propagation speed. The jet structures behind the jet head or CD are also different for different compositions. We have also plotted the corresponding contours of the adiabatic index (Γ) for Models A1–A4 in Figures 4(a)–(d). The beams of the jets with non-zero baryons (i.e., panels (b), (c), and (d)) are much hotter ($\Gamma \sim 4/3$), while the jet beam of pair-plasma jet (panel (a)) has regions where the jet becomes colder and the adiabatic index reaches values $\Gamma \sim 1.5$. The cocoon region is very hot for the baryonic jets but not so hot for the pair-plasma jet. It was pointed out by Chattopadhyay & Ryu (2009) that electron–positron plasma is thermally less relativistic (i. e., rest mass

energy greater than the thermal energy), which is also shown in Figure 2(a). Since these simulations are for thermally-driven jets, the electron–positron jet is slowest and is less hot. This is also clear from the enthalpy column of Table 1, where h_j is greatest for the jet with $\xi = 0.2$ (Model A2). Consequently, the jet kinetic power ($\propto h$) will be highest for the jet of Model A2 and lowest for Model A1. It was also pointed out by Chattopadhyay & Ryu (2009) and also from Table 1 of this paper that the electron-proton jet is not the most relativistic.

3.4. Model B: Equal Enthalpy Models

In Model A, we launched jets with the same injection parameters but different compositions of the flow changed the enthalpy of the jet. The specific enthalpy is related with the jet
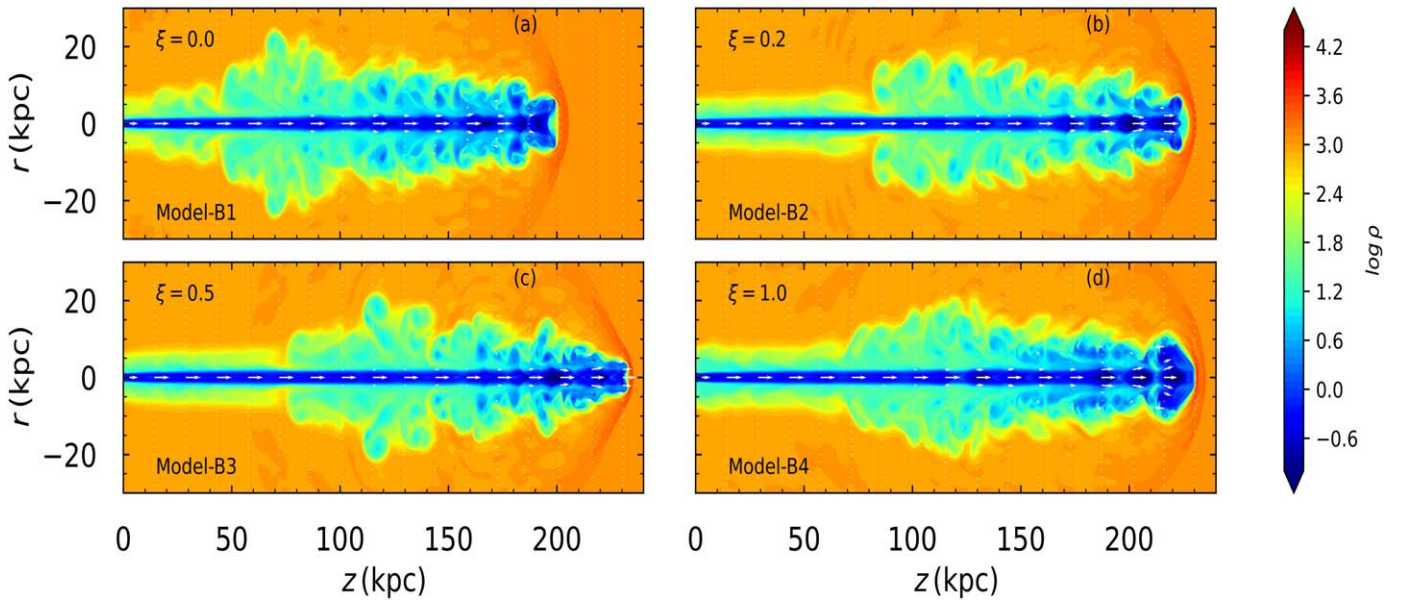
Figure 5. The density contours along with velocity vectors for various compositions. The specific enthalpy is kept same for all the jet Models B1–B4.

kinetic luminosity by

$$L_j = \gamma^2 \rho h \pi R_b^2 v_j \quad \text{erg s}^{-1} \qquad (8)$$

which can be written as

$$L_j = \gamma^2 \left(\frac{\rho_a}{\eta}\right) h \pi R_b^2 v_j \quad \text{erg s}^{-1}; \qquad \eta = \rho_a / \rho_j. \qquad (9)$$

Since the injection velocity is exactly the same for all of the models in this paper, from Equation (8), a jet with higher values of h_j (injected value of h) will have higher values of L_j. Therefore, it is no wonder that the jet's morphology will depend on its composition. Consequently, in Model A, although the injection parameters are exactly the same, the composition is different and so the jets corresponded to different jet power L_j. We found that the jet with $\xi = 0.2$ has the highest L_j for this value of h_j. It is expected that a jet with higher kinetic luminosity will produce higher propagation speeds, and even the structures that are formed are influenced by L_j (Massaglia et al. 2016; Rossi et al. 2020; Seo et al. 2021). Hence, to check for the effect of composition, we tune the value of Θ_j in such a way that all of the models with different compositions have the same specific enthalpy, and therefore have the same jet power. Assuming the ambient medium density of the order of $10^{-4} m_p$ cm^{-3} (Ferrari 1998), we have calculated the jet power for all of the models, which is given in Table 1.

In Figures 5(a)–(d), density contours and velocity vectors are plotted at $t = 8.0$ Myr for the jet Models B1–B4. The injection parameters correspond to the stars in Figure 2(b). We show that the propagation speeds and the structures formed by the jets even after fixing the jet kinetic power differ with a change in composition. In comparison to other plasma compositions, $\xi = 0.0$ shows a higher number of turbulent structures. The jet head area is narrower for composition $\xi = 0.5$ in comparison to other models. Once again, the propagation speed of the jet with $\xi = 0.0$ is the slowest. However, in this particular case the $\xi = 0.5$ jet is the fastest, followed by $\xi = 1.0$. Interestingly, out

of the four different models of a jet with the same enthalpy, $\xi = 0.5$ has the strongest recollimation shock (compression ratio $= 41$, measured along the axis), while $\xi = 0.2$ has the strongest reverse shock (compression ratio $= 16.7$, measured along the axis). In Figures 6(a)–(d), we have plotted the contours of Θ. The Θ distribution shows the locations of hot-spots for these models. The temperature contours show that the locations and also the areas of the hot-spots are different for these models. The structure of the Mach disk changes for different compositions.

3.5. Model C: Same Mach Number Jets

The structure of the cocoon crucially depends on the Mach number of the jet. So, it is expected that the structure of the jet head and the cocoon will be different if the Mach number of the jet beam changes. In Model B, the Mach numbers of the jets were different, although the jet power was the same. We will now investigate the case when the injected value of the Mach number of the jet is kept same for different values of composition. The value of Θ_j for Models C1–C4 is tuned in such a way that the injected value of the sound speed of the jet-beam remains the same in every model, even after the variation in the composition parameter. Since all of the jets are also launched with the same velocity, in this case it implies that they are also launched with the same Mach number. The value of Θ_a is also tuned such that the value of the local sound speed in the ambient medium is the same for all of the models. The injection parameters of Models C1–C4 correspond to the stars in Figure 2(c). The contours of log γ at $t = 11.6$ Myr are plotted in Figures 7(a)–(d) for these simulations. The locations of the recollimation shock in the jet beam are most clearly visible in this figure. The FS is the leading blue curve. The jet head or CD has a dimple for the $\xi = 1.0$ jet (Model C4). The propagation speed of the $\xi = 0.0$ jet is the slowest, while those due to $\xi = 0.5$ and $\xi = 0.2$ are similar.

It is intuitive that the jet will lose speed as it wades through the ambient medium due to the resistance offered by the medium. However, a large number of numerical simulations have shown that for some initial conditions, jets can be
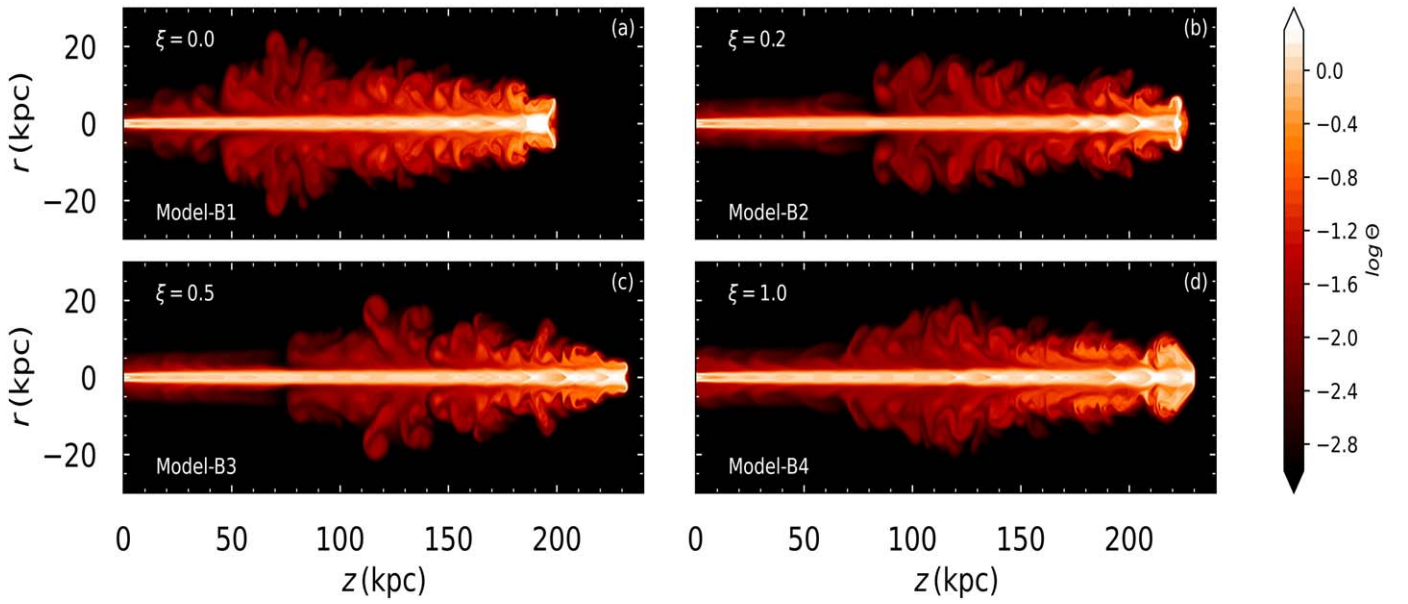
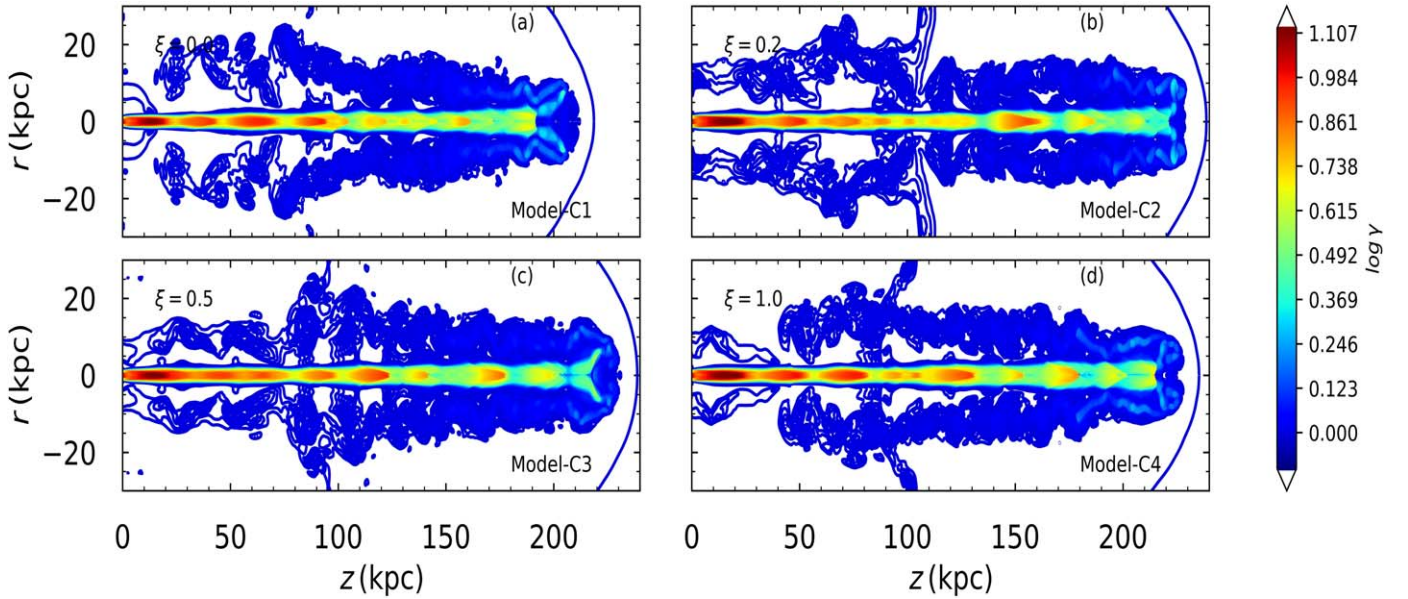**Figure 6.** The temperature (Θ) contours for Models B1–B4.

Figure 7. The contours of the Lorentz factor for Models C1–C4.

accelerated above the injected Lorentz factor by a significant margin. One of the simplest but very strong hydrodynamic boosters was suggested by Aloy & Rezzolla (2006). The production of a strong rarefaction wave near the contact discontinuity accelerates the jet with an increase in overall propagation speed (Aloy et al. 2005; Hervet et al. 2017). In addition, the formation of many recollimation shocks (RCSs) within the jet beam may locally decelerate the flow, but the associated rarefaction fan (RF) may enhance the local speed of the jet. To highlight this, we have plotted the local Lorentz factor along the z-axis, i.e., $\gamma(0, z)$ (Figure 8(a)) and density $\rho(0, z)$ (Figure 8(b)) as a function of z. The panels (top–bottom) in columns (a) and (b) of Figure 8 show the variation of Lorentz factor and density for Models C1 ($\xi = 0$)–C4 ($\xi = 1.0$), respectively. In the top panel of 8(b), we have marked the positions of FS, RS, RCS, and RF. The Lorentz

factor is boosted to a value higher than the injected value in the first RF for all of the models. Likewise, all of the sharp jumps in density and the Lorentz factor are the locations of internal shocks in the beam. The rarefaction fans are the regions between two internal shocks, as shown in Figure 8(b). The rarefaction wave is an expansion wave; hence, the velocity/ Lorentz factor increases in this region, which is clearly visible. So there would be alternate denser and rarer regions, and correspondingly slower and faster regions within the jet beam. Therefore, if an RCS and RF combination forms near the jet head, then the propagation speed should also be higher. In Figure 9(a), we plot the jet head positions on the jet axis as a function of time for the four jets described in Models C1–C4. In Figure 9(a), we plot the corresponding jet head velocity v_{jh} as a function of time. From the jet head positions, it is clear that the $\xi = 0.0$ jet (Model C1) is the slowest. Out of the four jets,
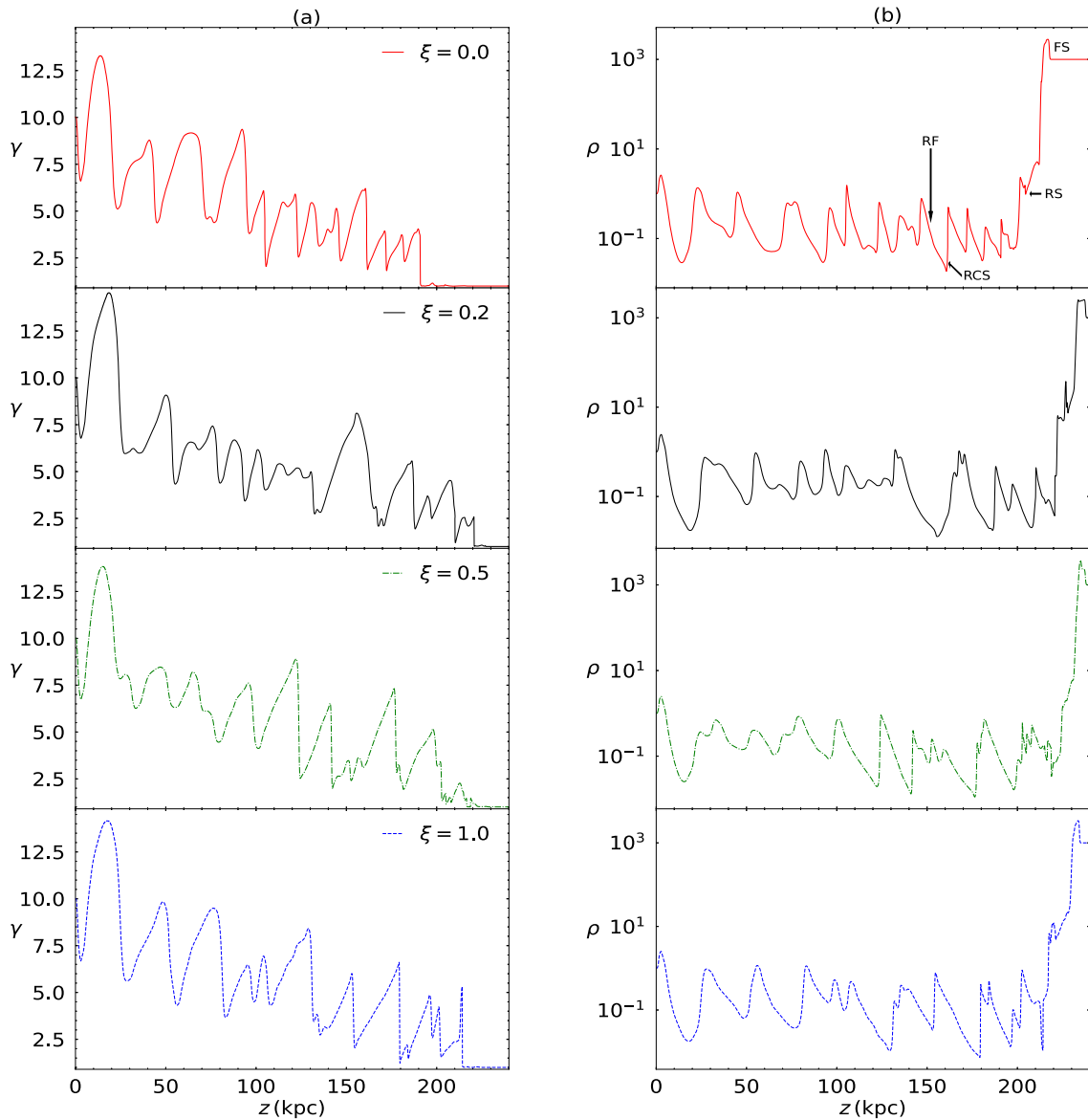
Figure 8. (a) Jet Lorentz factor γ and corresponding (b) ρ as a function of z for different jet compositions at $t = 11.6$ Myr. FS, RS, and the recollimation shock (RCS) are marked in the top most panel of column b. The flow variables along the spine of the jet corresponds to Models C1–C4.

$\xi = 1.0$ (Model C4, blue dashed) is slower than the other two jet types. For these injection parameters, the jets decelerate at some time (around 2 Myr for $\xi = 0.0$ jet) but then reaccelerate (around 4 Myr for $\xi = 0.0$). These are due to the formation of a combination of RF-RCS near the jet head. For the jets containing baryons, this reacceleration is somewhat at an earlier time. The deceleration and reacceleration of the jets are also clear from Figure 9(b), where we plot the velocity of the jet head surface along the jet axis. Although the propagation speed of the pair-plasma jet is overall lower, it can overshoot the speed of the jet head for other baryon containing jet.

4. Discussion and Conclusions

4.1. Discussion

The morphology of thermally driven relativistic jets has been studied by several authors (Martí et al. 1997; Scheck et al. 2002; Mizuta et al. 2004); each author focuses on large-scale evolution and dynamics of relativistic jets. In this paper, we

have investigated the propagation of relativistic jets through a uniform ambient medium using an approximate but analytical relativistic equation of state (CR EoS) by performing axisymmetric, relativistic, and hydrodynamic simulations in cylindrical geometry. The code that we have used in this paper is based on Harten's TVD routine but adopted for relativistic hydrodynamics and relativistic EoS (Ryu et al. 2006; Chattopadhya et al. 2013). Since relativistic flows are hot, ionized, and can be thermally transrelativistic, the fixed Γ EoS is not compatible with the physics of the flow. A relativistic plasma is composed of electrons and ions, and the information of the constituent particles is in the EoS. Meanwhile, the EoS appears in the expression of state variables, such as momentum density and energy density of the flow. Therefore, the evolution of the flow should also depend, in addition to other things, on the composition. The effect of composition has been shown in the case of accretion onto compact objects (Chattopadhyay & Ryu 2009; Chattopadhyay & Chakrabarti 2011; Chattopadhyay & Kumar 2016; Sarkar et al. 2020). To reduce the number of
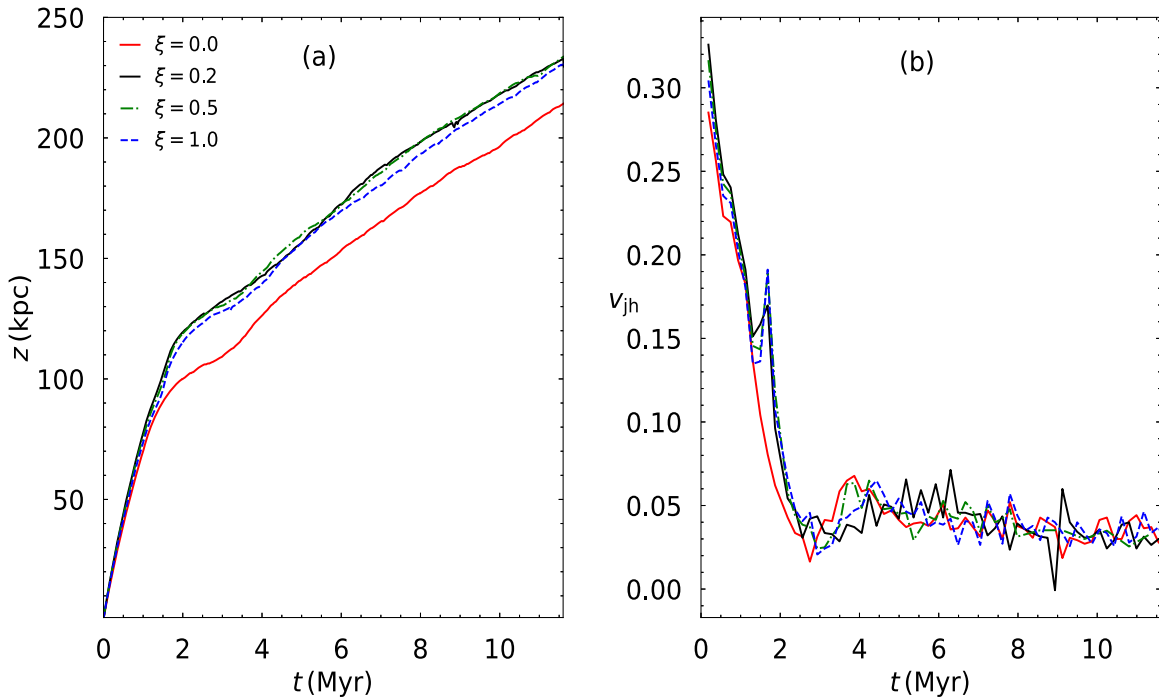
Figure 9. (a) Jet head position and (b) jet head velocity v_{jh} as a function of t for different jet compositions. The compositions marked in panel (a) correspond to Models C1–C4.

free parameters, we fixed the injection velocity $v_j = 0.995$ for all of the models. We also fixed the jet cross section and the ambient medium density for all of the models. Initially, we ran a generic jet simulation for an electron-proton ($\xi = 1.0$) jet (Model OD) and showcased the generic features such as the FS, CD, and RS, the back-flowing jet material, and the formation of various recollimation shocks along the beam of the jet. We then considered Models A1–A4, which all started with the same Θ_j but took four different values of ξ. In Figure 2(a), the injection parameters are the stars on the curve, and the adiabatic indices Γ_j and the corresponding sound speeds are different. This means that the eigenvalues of the flow will differ for jets with different compositions. Therefore, the eventual evolution of the jets with different compositions would be different in terms of propagation speed. The structure of the jet is shown in Figures 3 and 4. The adiabatic index or Γ contour plots also show that the interaction determines the value of the adiabatic index along the jet beam and also in the cocoon. The electron-positron jets show a lot of structure and are generally colder (Γ values are higher). In Models B1–B4, jets with the same enthalpy are launched (stars in Figure 2(b)). Since they all start with the same injection velocity, all of these jets are launched with the same jet kinetic power. Even in this case, the propagation velocities and detailed structures depend on the composition parameter ξ. The jet with $\xi = 0.5$ is the fastest and $\xi = 0.0$ is the slowest, and turbulent structures are more pronounced compared to jets containing protons. In the recollimation shock regions, the density enhanced regions appear to coincide with the hot regions but not so in the jet-head region. This would have an interesting effect on the brightness and spectral morphology of the jets. The number of collimated shock regions is also higher when compared to the $\xi = 0.0$ jet. In Models C1–C4, jets launched with the same Mach number but different compositions are investigated. The Lorentz factor contours exhibited the recollimation shocks

more vividly. With these injection values, the $\xi = 0.2$ and the $\xi = 0.5$ attain comparable speed, although the structures are different. The jet head structures are also different: the electron-proton jet head shows an inward dimple. In fact between $t = 2$–4 Myr, the $\xi = 0.0$ jet head speed exceeds that due to all of the other proton containing jets. However, the initial inertia of the proton carrying jets keeps these jets ahead of the pair-plasma jet. We have compared jets with the same injection parameters, same enthalpy and injection speed, and same Mach number and injection speed but with different compositions. Since the information of composition is in the local enthalpy of the jet, the evolution of the jet in terms of propagation speed, or the number of recollimation shocks, or the structure of the Mach disk and so on depends on the composition. However, the basic structure of a jet with a forward shock, jet head (or contact discontinuity), and a reverse shock is seen for jets of all compositions. Additionally, we have performed two-dimensional axisymmetric simulations of jets, but the recent three-dimensional simulations (Rossi et al. 2020; Seo et al. 2021) highlight that differences in dimensionality can lead to different physical outcomes. One may study the non-axisymmetric interaction of jets with the ambient medium, which may produce more complex structures. Given that an energy cascade to smaller scales is not possible in two-dimensions, the properties of turbulence in three-dimensional simulations are radically different (Massaglia et al. 2016). Hence, three-dimensional simulations can provide more realistic and complex results to quantify the effect of composition on the dynamics and structures of these jets.

4.2. Conclusions

Numerical simulation of a relativistic jet requires a time-dependent study of a supersonic, relativistic beam of matter flowing through a denser, colder medium. From a large number of simulations, it is common knowledge that jets launched with

the same injection parameters should evolve identically. However, our results (Models A1–A4) show that despite fixing the injection parameters, jets with different compositions show a difference in terms of propagation speeds and also the structures formed by the jets. The electron–positron jets are less relativistic (less hot and slower) than jets with all other composition parameters. We also studied jet models (B1–B4) with same kinetic luminosity but with different plasma compositions. Even after fixing the kinetic luminosity of the jet, we found out that the propagation velocities are different and the jet with $\xi = 0.5$ turned out to be the fastest and the jet composed of pair plasma is slowest. The boosting mechanisms are important aspects of multi-dimensional jet simulations and the jets launched with the same initial Mach number (Models C1–C4) show that the reacceleration epochs vary with a change in the composition parameter. The electron–positron jets can overshoot the speed of the jet-head for other baryon containing jets, but overall it remains slower than the jets containing baryons. It may be noted that although we have chosen initial flow parameters for different models that did not cause widely different injection values (L_j, h_j etc. are close by), there is still a notable difference between the pure leptonic and jets with baryon content. These conclusions might have been different if we had chosen other parameters. For example, in Figure 2 (a), the Θ_j chosen keeps the $\xi = 0.2$ jet as thermally most relativistic, but at lower Θ_j flows with other ξ might be more relativistic. All these cases show that the composition of the jet is important in the eventual propagation and morphology of the jet, and it cannot be predicted or parameterized a priori.

ORCID iDs

Raj Kishor Joshi ● https://orcid.org/0000-0002-9036-681X
Indranil Chattopadhyay ● https://orcid.org/0000-0002-2133-9324

References

Aloy, M. A., Janka, H. T., & Müller, E. 2005, A&A, 436, 273
Aloy, M. A., & Rezzolla, L. 2006, ApJL, 640, L115
Blandford, R. D., & Rees, M. J. 1974, MNRAS, 169, 395
Bromberg, O., Nakar, E., Piran, T., & Sari, R. 2011, ApJ, 740, 100
Chandrasekhar, S. 1939, An Introduction to the Study of Stellar Structure (Chicago, IL: Univ. Chicago Press)
Chattopadhya, I., Ryu, D., & Jang, H. 2013, in Astronomical Society of India Conf. Ser. 9, ed. K. Pushpa & C. H. Ishwara-Chandra (Bangalore: BAIS), 13
Chattopadhyay, I., & Chakrabarti, S. K. 2011, IJMPD, 20, 1597
Chattopadhyay, I., & Kumar, R. 2016, MNRAS, 459, 3792
Chattopadhyay, I., & Ryu, D. 2009, ApJ, 694, 492
Duncan, C., Hughes, P., & Opperman, J. 1996, in ASP Conf. Ser. 100, Energy Transport in Radio Galaxies and Quasars, ed. P. E. Hardee, A. H. Bridle, & J. A. Zensus (San Francisco, CA: ASP), 143
Duncan, G. C., & Hughes, P. A. 1994, ApJL, 436, L119
Falle, S. A. E. G., & Komissarov, S. S. 1996, MNRAS, 278, 586
Fanaroff, B. L., & Riley, J. M. 1974, MNRAS, 167, 31P
Ferrari, A. 1998, ARA&A, 36, 539
Hardcastle, M. J., & Krause, M. G. H. 2014, MNRAS, 443, 1482
Harten, A. 1983, JCoPh, 49, 357
Hervet, O., Meliani, Z., Zech, A., et al. 2017, A&A, 606, A103
Joshi, R. K., Chattopadhyay, I., Ryu, D., & Yadav, L. 2021, MNRAS, 502, 5227
Joshi, R. K., Chattopadhyay, I., & Yadav, L. 2022a, MNRAS, 509, 85
Joshi, R. K., Debnath, S., & Chattopadhyay, I. 2022b, ApJ, 933, 75
Kawakatu, N., & Kino, M. 2006, MNRAS, 370, 1513
Keppens, R., Meliani, Z., van der Holst, B., & Casse, F. 2008, A&A, 486, 663
Komissarov, S., & Porth, O. 2021, NewAR, 92, 101610
Komissarov, S. S. 1994, MNRAS, 266, 649
Marti, J. M., Mueller, E., & Ibanez, J. M. 1994, A&A, 281, L9
Martí, J. M., Müller, E., Font, J. A., Ibáñez, J. M. Z., & Marquina, A. 1997, ApJ, 479, 151
Massaglia, S., Bodo, G., Rossi, P., Capetti, S., & Mignone, A. 2016, A&A, 596, A12
Mathews, W. G. 1971, ApJ, 165, 147
Mignone, A., Plewa, T., & Bodo, G. 2005, ApJS, 160, 199
Mignone, A., Rossi, P., Bodo, G., Ferrari, A., & Massaglia, S. 2010, MNRAS, 402, 7
Mioduszewski, A. J., Hughes, P. A., & Duncan, G. C. 1997, ApJ, 476, 649
Mizuta, A., Yamada, S., & Takabe, H. 2004, ApJ, 606, 804
Norman, M. L., Winkler, K. H. A., Smarr, L., & Smith, M. D. 1982, A&A, 113, 285
Rossi, P., Bodo, G., Massaglia, S., & Capetti, A. 2020, A&A, 642, A69
Ryu, D., Chattopadhyay, I., & Choi, E. 2006, ApJS, 166, 410
Sarkar, S., & Chattopadhyay, I. 2022, JApA, 43, 34
Sarkar, S., Chattopadhyay, I., & Laurent, P. 2020, A&A, 642, A209
Scheck, L., Aloy, M. A., Martí, J. M., Gómez, J. L., & Müller, E. 2002, MNRAS, 331, 615
Seo, J., Kang, H., & Ryu, D. 2021, ApJ, 920, 144
Singh, K., & Chattopadhyay, I. 2019, MNRAS, 486, 3506
Synge, J. 1957, The Relativistic Gas (Amsterdam: North-Holland Publishing Company)
Walg, S., Achterberg, A., Markoff, S., Keppens, R., & Meliani, Z. 2013, MNRAS, 433, 1453